AMBER, I. and O'DONOVAN, T.S. 2017. Heat transfer in a molten salt filled enclosure absorbing concentrated solar radiation. *International journal of heat and mass transfer* [online], 113, pages 444-455. Available from: https://doi.org/10.1016/j.ijheatmasstransfer.2017.04.028

Heat transfer in a molten salt filled enclosure absorbing concentrated solar radiation.

AMBER, I. and O'DONOVAN, T.S.

2017

© 2017 Elsevier Ltd.

This document was downloaded from https://openair.rgu.ac.uk

Heat transfer in a molten salt filled enclosure absorbing concentrated solar radiation

I.Amber and T.S.O'Donovan

Institute of Mechanical Process and Energy Engineering
Heriot-Watt University, Edinburgh,
EH14 4AS, United Kingdom
Corresponding author: I.Amber, Email: amberity@yahoo.com

Abstract

Numerical simulations of the natural convection driven by the direct absorption of concentrated solar radiation by a high temperature molten salt filled enclosures for height to diameter ratios (H/D) of 0.5, 1 and 2 and Rayleigh numbers 10^7- 10^{11} is presented. The domain of interest consists of a fluid cavity bounded by rigid adiabatic vertical walls, a heat-conducting bottom wall of finite thickness and an open adiabatic top surface, directly irradiated by a non- uniform concentrated solar flux. The salt volume is first heated non-uniformly by direct absorption of solar radiation and subsequently from the lower absorber plate which is heated by the absorption of the radiation transmitted through the salt.
A Finite Element Method is used to solve the time dependent two dimensional Navier Stokes equations that includes a depth dependent volumetric heat source and temperature dependent thermophysical of molten salts.
Numerical results presented in terms of isotherms and streamlines show a nonlinear temperature profile consisting of distinct layers where thermocapillarity and buoyancy effects are evident. Fluid flow development in the lower layer is found to vary significantly with time and exhibits an initial stage, transitional stage and quasi-steady stages. The magnitude of the natural convection and the duration of each stage is found to decrease as the aspect ratio increases from 0.5 to 2. Calculation of the average heat transfer reveals that the Nusselt Rayleigh number relationship is not uniformly linear and the average heat transfer over the lower boundary surface increased with increasing Ra.

Keywords: Natural convection, Numerical simulation, Molten salt

1. Introduction

Natural convection plays an important role in design, performance and operating costs in many engineering systems and physical applications. In applications such as buildings, power generation, thermal storage, environmental sciences and electronics cooling, natural convection has been found to strongly influence the operating temperatures and temperature fields [1, 2]. natural convection induced by absorption of solar radiation occurring shallow regions of oceans and lakes [3, 4] has been found to have significant influence on the fluid temperature distribution, biological activity and water quality due to the mixing of pollutants and sediments.
In the present study numerical simulations are considered for the natural convection in an enclosure containing molten salt (KNO_3-$NaNO_3$) subject solar radiative heating. The principal driving force for the circulation of the fluid comes from the heat exchange from the wall of finite thickness located at the lower boundary.

Natural convection induced by absorption of solar radiation occurring shallow regions of oceans and lakes [3, 4] has been found to have significant influence on the fluid temperature distribution, biological activity and water quality due to the mixing of pollutants and sediments.
The present study is motivated by the interest to understand heat and fluid flow interactions and their dependences on defined control parameter within a novel small scale solar thermal store. The thermal store accomodates a heat conducting absorber plate of finite thicknes at the lower boundary which promotes isothemalisation required to maximise the storage capacity without damaging the storage medium, which can typically sustain temperatures up to 600^oC [5, 6]. KNO_3-$NaNO_3$ salt (60-40 wt%, m.p. 222^{o}C) has been used up to 565^{o}C in solar thermal energy collection and storage applications, where its thermal stability has been successfully demonstrated without significant degradation [7–10].
Investigation of the interaction between heat transfer and fluid flow in convective thermal transport in many physical systems has been of primary interests since the classical works of Rayleigh and Bernard [11, 12]. Cavities with differentially heated isothermal or iso-flux end walls have formed idealised models for conducting the fundamental studies for understanding these interactions [11, 12]. The differentially heated cavity problem has been ex-

tensively studied experimentally and numerically in various contexts (aspect ratios, geometries, orientation, fluids and control parameters) and several boundary conditions. A large body of literature exists for natural convection in differentially heated cavities; three main thermal boundary conditions exists based on heating phase angles, ϕ [11–13]: (i) Heating from below ($0^o < \phi < 90^o$), typical Rayleigh Bernard flows (ii) Lateral heating from the side (ϕ=90^o) problem and (iii) heating from above ($90^o < \phi < 180^o$). In these problems steady state solutions are obtained for idealised isothermal or flux boundaries conditions by time stepping from a prescribed initial state.

Unlike in the differentially heated cavity problem, for radiation induced natural convection problems, it is of fundamental significance to understand the heat and flow behaviour in an enclosure under time dependent heating conditions.

Literature relating to the fluid mechanics and heat transfer interaction in enclosures, where the primary driving force for the natural convective motion, is the volumetric absorption of thermal energy is very limited particularly in high temperature fluids. Webb and Viskanta [14, 15] investigated the natural convection in rectangular domains heated by radiative flux at a vertical surface. In the studied domain the primary driving force for the natural convective motion is the volumetric absorption of thermal energy. For two aspect ratios, thin hydrodynamic boundary layers, a stagnant and stratified central core and convective flow regimes were revealed. The thin thermal boundary observed at the vertical walls is associated with a low heat transfer near the base and high heat transfer at the top of the enclosure. The maximum fluid temperature in the cavity increased with increasing aspect ratio. The flow structure revealed a loss of centrosymmetry (eddy centre) characteristic of natural convection flows in cavities with differentially heated walls due to the direct heating of the core of the flow by solar radiation within the fluid.

Li and Durbetaki [16] carried out numerical investigations on the radiation induced transient natural convection boundary layer. In the study a vertical surface of a non-reactive semi-infinite solid was suddenly subjected to a radiative heat flux source. The time required for the surface temperature to attain a specified value and drive natural convection was inversely proportional to the square of the radiative heat flux. Onyegebu [17] numerically demonstrated that natural convection in a rectangular domain subjected to isotropic radiation at the top surface is developed at low fluid depths and albedo, while large fluid depths and low surface boundary emissivity suppressed natural convection. Verevochkin and Startsev [18] in a rectangular domain numerically studied thermal convection in a horizontal water layer cooled from the top and absorbing incident solar radiation. The study identified three different heat transfer regimes: intermittent convection, steady state convection and free convection where flow transition were found to occur at different values for ratios of the downward solar radiation flux at a depth to heat flux through the interface [18]. Numerical [19–22], experimental [23, 24] and scaling [25–27] investigations of the unsteady natural convection induced by the absorption of radiation in triangular enclosures have been reported. These have relevance to the daytime natural convection in a side arm and in littoral regions in large water bodies. These investigations report distinct driving mechanisms and flow regimes described as: early flow transition characterised by the thermal boundary layer development, a transitional stage marked by the existence of irregular occurring rising plumes and a quasi-steady state stage.

Recently, Hattori et al. [28, 29] and Harfash [30] performed three dimensional numerical simulations of convection induced by the absorption of radiation. In the former, the authors applied a Direct Numerical Simulations (DNS) technique to simulate direct absorption of radiation in a parallelopiped relevant to deep water bodies subjected to a top solar radiative heating, where the authors state that investigations are scarce. Results revealed a non-linear temperature profiles where two distinct layers: an upper stratification region, due to internal heating, provided by the direct absorption of radiation and a potentially unstable boundary layer due to the absorption and re-emission of the residual radiation by the bottom surface are found. The influence of a non-linear temperature stratification on maximum height thermal plumes and the mixing driven by rising thermal plumes. Theoretical calculations to determined the lower mixed layer thickness was presented. Harfash [30] conducted three dimensional numerical simulations of convection induced by absorption of radiation based on linear and non linear analysis. The study reports the linear theory does not predict anything about instability and only provides boundaries for instability because of the presence of non-linear terms. However the non-linear stability theory was demonstrated to overcome the limitations of the linear stability theory and as such is highly desirable, for full assessment of any subcritical regions.

This paper presents two dimensional numerical simulations for the transient natural convection in a fixed volume of binary molten KNO_3-$NaNO_3$ absorbing concentrated solar radiation in enclosures of height to diameter ratios (H/D) of 0.5, 1 and for Rayleigh numbers 10^7 - 10^{11}. The present model accounts for the depth dependent absorption of solar radiation by assuming, the attenuation coefficient is characterised by a single bulk attenuation coefficient, which is a common practice found in many literatures.

2. Geometry and numerical formulation

Figure 1, shows a two dimensional schematic of the physical model for an aspect ratio (H/D=1). The enclosure contains molten KNO_3-$NaNO_3$ confined between rigid, adiabatic vertical walls and a rigid lower boundary wall of finite thickness in contact with the molten salt. The top surface is stress free, open and adiabatic. The sole purpose of the plate located at the lower boundary is to absorb all radiation transmitted to the lower surface, subsequently driving a natural convection to heat and mix the molten salt.

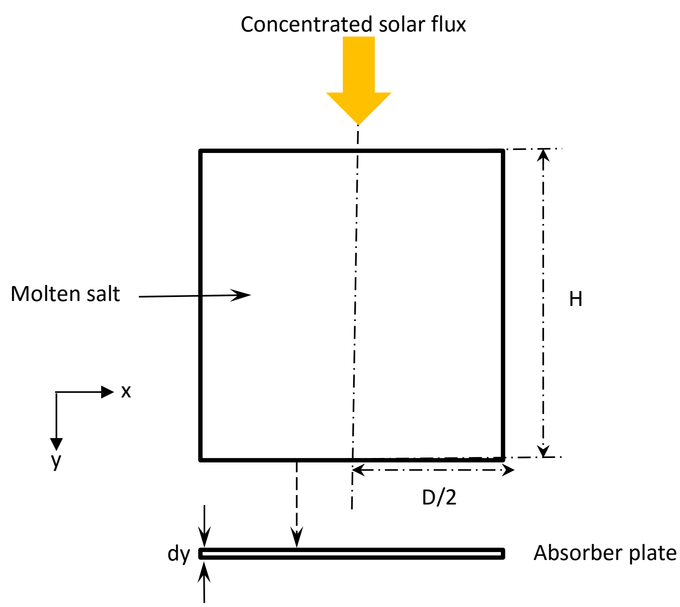

Figure 1: Physical model

KNO_3-$NaNO_3$ (60%-40% wt) [31] commonly used in sensible heat is assumed to be initially in a liquid and quiescent state and at a temperature, T_0=250^{o}C, above its crystallisation temperature. The molten salt is assumed to remain in a molten state for this study.

At the time t=0, a non-uniform concentrated flux at (700X) is initiated at the top surface and thereafter maintained.
The solar radiation intensity penetrating downward into the fluid depth absorbed directly in a non uniform manner is described mathematically by equation (1)

$$I = CAI_0 e^{(\alpha y)} \tag{1}$$

where I is the intensity transmitted through a layer of material of thickness y, I_0 is the radiation intensity at the surface y_0, and α is the solar weighted absorption coefficient and y represents the vertical coordinate. The volumetric rate of heat generated can be estimated by:

$$S = \frac{dI}{dy} \tag{2}$$

In the present study the non absorbed solar radiation reaching the bottom surface is assumed to be fully absorbed by a black conducting wall of finite thickness located at the bottom boundary. The heat exchange at the lower boundary provides the principal driving force for the fluid circulation.

3. Governing Equations

It is assumed in the present analysis that the molten KNO_3-$NaNO_3$ is Newtonian with temperature dependent properties. Flow is assumed to be two-dimensional and the fluid top surface is assumed to be optically smooth and intercepts non uniform concentrated solar flux defined as a Gaussian profile.
The generated temperature and flow fields within the enclosure are governed by the continuity, momentum and energy transport equations with a source term as given below equations (3) to (5):

$$\nabla \cdot \overrightarrow{V} = 0 \tag{3}$$

$$\rho \frac{\partial(\overrightarrow{V})}{\partial t} + \rho(\overrightarrow{V} \cdot \nabla) \cdot \overrightarrow{V} = -\nabla p + \mu \nabla^2 \overrightarrow{V} + \rho g \tag{4}$$

$$\rho C_p \Big(\frac{\partial T}{\partial t} + \nabla \cdot \overrightarrow{V} T \Big) = \nabla \cdot (k \cdot \nabla T) + S \tag{5}$$

where $\overrightarrow{V}$ is the velocity vector consisting of the velocity components u and v. T is the spatial temperature in the domain; P is the pressure; S is the source term representing the rate of absorption of solar radiation given in a simple form in equation (6) determined by solving the Radiative Transfer Equation (RTE) subject to the appropriate radiative boundary conditions and neglecting wavelength dependency, scattering and directional cosines. Thermo physical properties of molten salt KNO_3-$NaNO_3$ (40-60%wt) are taken for temperature dependent properties which is given in Table 1.

$$S = [1 - \rho_a]\alpha I(e^{\alpha y} + \kappa e^{\alpha L}) \tag{6}$$

The first terms on the RHS of equation (6) represent the contributions of the direct absorption of radiation within the fluid body while the second term denotes the contribution to the heated absorber plate at the bottom. Using the following scales: H $\sim$ α (length scale); t $\sim$ κ α ^{2} (time scale); T $\sim$ g β I_0/C_p κ α ^{2} (temperature scale); $\overrightarrow{V}$=(u,v), $\sim$, κ α (velocity scale), equation (3) to (5) are non dimensionalised as:

$$\rho\frac{\partial(\overrightarrow{V})}{\partial t} + \rho(\overrightarrow{V} \centerdot \nabla)\overrightarrow{V}) = -RaPr\nabla p + RaPr\nabla^2\overrightarrow{V} + PrRaT \tag{7}$$

$$\rho C_p\Big(\frac{\partial T}{\partial t} + \nabla.\overrightarrow{V}T\Big) = \nabla \centerdot (k \centerdot \nabla T) + S \tag{8}$$

The controlling parameters describing the flow in an enclosure are given by the Rayleigh number defined in terms of flux Rayleigh number is given as shown by equation (9).

$$Ra = \frac{\rho^2 C_p g\beta q H^4}{\mu k^2} \tag{9}$$

where g, ρ, μ, k, and β are the gravity, density, viscosity thermal diffusivity and volumetric expansion constant respectively.
The Prandtl number (equation 10) is a fluid property:

$$Pr = \frac{\mu C_p}{k} \tag{10}$$

The aspect ratio is defined as shown in equation (11)

$$A = \frac{H}{D} \tag{11}$$

where H and D are the height and width. The volume remains constant for all aspect ratios.

The dimensionless heat transfer is defined in equation (12)

$$Nu = \frac{qD}{k\Delta T} \tag{12}$$

From the transient analysis, the initial conditions are set as follows:

1. u,v(t=0)=0.
2. T(t=0)=250K melting point temperature of salt t$\leqslant$0.

The Boundary conditions are summarised as:

1. Vertical wall is rigid adiabatic, and impermeable. No slip occurs at the side walls. The velocity components and normal temperature gradients being zero, (u=v=dT/dn=0).
2. The top boundary (y=0) is a stress free and adiabatic surface. (du/dx=dv/dy=dT/dy=0)
3. The lower boundary is a rigid wall with no slip (u=v=0) and of finite thickness and thermal conductivity, where the transmitted flux to this surface is absorbed and heats the lower fluid at temperatures obtained from equations (13). The temperature of the bottom y=-H is given by:

$$T(t) = T_i + \Delta T \tag{13}$$

where, $\Delta \mathrm{T} \sim \frac{2I}{k}\left(\sqrt{\frac{\alpha t}{\pi}}\right)^{\frac{1}{2}}$ I is the Total Solar Intensity(TSI) and α is a weighted attenuation coefficient.

Table 1: Thermopysical properties of molten KNO_3-$NaNO_3$ salt and properties of absorber plate material [34, 35]

Property/units	**KNO_3-$NaNO_3$**	**Copper**
ρ (kgm^{-3})	2090-0.636T	8960
k(W (mK)$^{-1}$)	0.443+1.9 $\times$ 10^{-4}T	400
C_p (J(kgK)$^{-1}$)	1443-0.172T (1396.044+0.172T)	385
μ (kg(ms)$^{-1}$)	22.714-0.12T+2.281$\times$10^{-4}T-1.474$\times$10^{-7}T	

3.1. Numerical implementation

The derived time dependent system of non-linear partial differential equations (PDEs) were solved using commercially available Finite Element Method

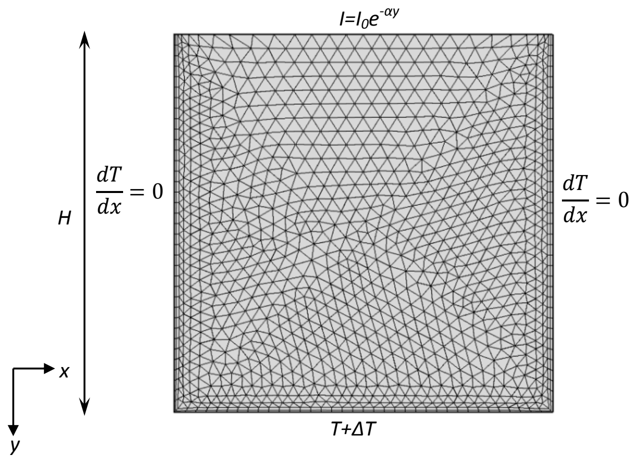

Figure 2: Unstructured computational mesh used in the present study.

(FEM) software COMSOL Multiphysics [32]. Second-order and linear elements discretisation were applied for the velocity and the pressure field, (P_2+P_1). An unstructured mesh consisting of triangular mesh elements is adopted in the simulation to account for the variability of the formed thermal plumes and its occurrence at arbitrary locations. Figure 2 shows a schematic of the unstructured mesh used in the numerical simulations for H/D=0.5, 1 and 2.

In order to ensure mesh-independent solutions, mesh convergence tests are performed. For a representative simulation for concentration ratio C = 700X, I_0= 1000 Wm^2, and α = 2 m^{-1} corresponding to the case Ra= 10^{11}, Figure 3 shows the results of the domain temperature across a mid-vertical plane for three different mesh resolutions for the cases of H/D= 0.5 (Figure 3a), 1 (Figure 3b) and 2 (Figure 3c). Based on the results of the mesh refinement, dimensionless mesh sizes of 0.01, 0.015, and 0.02 was used for H/D = 0.5, 1 and 2. Using these meshes it has been estimated that the relative error found between the solution at the finest mesh size was found to be below 2% for temperature solution and was adequate to optimize computational time without losing numerical accuracy.
Effect of time step on the solution were carefully examined for the numerical results. In Fig 4 the time-step dependence test for results of the time histories

for the vertical velocity for time steps: 0.2, 0.5, and 1 s tested is presented. For example example at H/D=1, three stages of the flow development can be seen. The solutions follow closely to each other, with slight differences among the solutions for the velocity and predicted flow transition times. In the present study, as a primary interest is to identify the thermal flow mechanism and development rather than resolve the details of convective instability and as a compromise between the computational time and the accuracy a time step of 1 s is adopted in the numerical calculation. This time step is found to be is sufficient to resolve and frequency component in the simulation. Similarly, the three stages of the thermal flow development

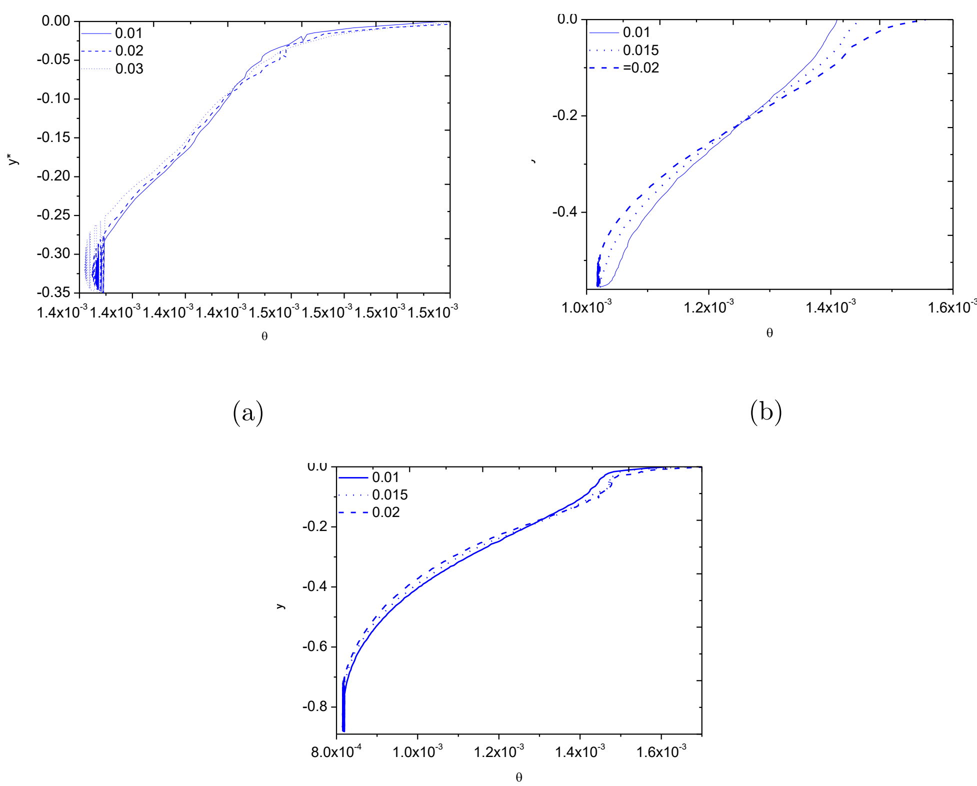

(a) (b)

(c)

Figure 3: Mesh convergence plot for the temperature taken from the vertical section at $\tau = 4.5 \times 10^{-3}$ (a) H/D=0.5 (b) H/D=1 (c) H/D=2.

observed is demonstrated in the solutions obtained at H/D =0.5 and 2. A convergence criteria of 10^{-5} was imposed for the residuals of the governing equation.

3.2. Validation

Due to lack of standard solutions for volumetric absorption of concentrated solar radiation in cylindrical enclosures, the model used in the present study is validated against, the laboratory-scale experiments of Lei and Patterson [23] for the natural convection in a horizontal fluid layer of shallow depth subject to constant and uniform radiation at the water surface. Numerically predicted temperature distribution along a vertical line is compared against the experimentally measured values from a water filled flow domain with measured bulk attenuation coefficient 6.16m illuminated by $I_0 = 50\text{W/m}^2$ at a reference temperature 21.5^oC, which gives $\text{Gr} = 2.51 \times 10^6$ and $\text{Pr} = 6.83$.

For full description of the laboratory experiment readers are referred to Lei and Patterson [23]. Fig 5 presents the results for the temperature distribution along the mid-height. The results obtained show a good agreement. Fig 6 shows a comparison of numerically simulated results and experimentally obtained transient temperature taken within a point in the boundary

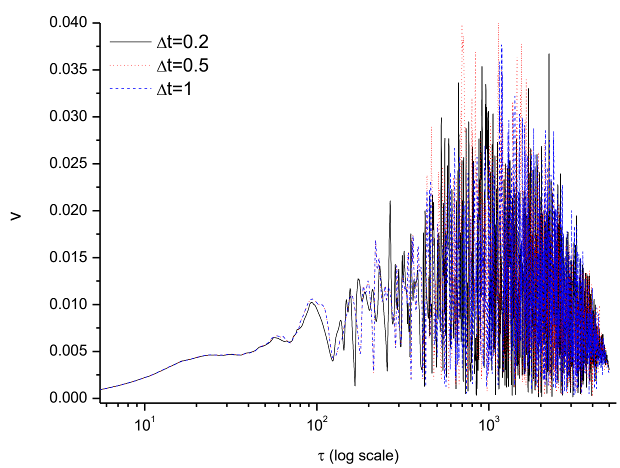

Figure 4: Mesh convergence plot for time history at H/D=1 for Ra= 10^{11}

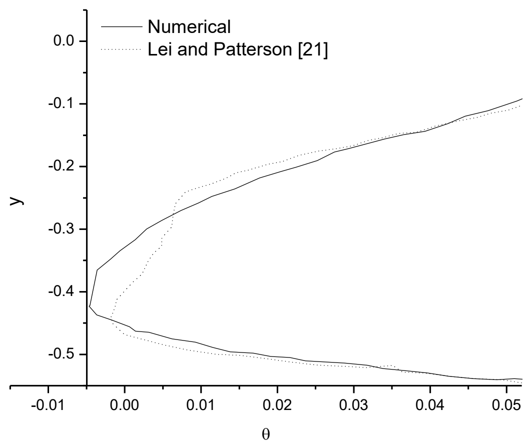

Figure 5: Vertical temperature profile at x=5.5 for experiments (dash) [23] and numerical simulation (solid) at $\tau = 0.200$ (5049s).

layer. From Fig 6, it can be seen that the comparison is satisfactory between results. The validation study demonstrates that the model is capable of predicting natural convection in enclosure subjected to solar radiative heating.

4. Results and discussion

Fig 4 to Fig 6 present isotherms and velocity streamlines for aspect ratio 0.5, 1 and 2 at dimensionless time steps $\tau = 2.27\times 10^{-5}$ (30s), $\tau = 1.82\times 10^{-3}$ (2290s), $\tau = 3.81\times 10^{-3}$ (4650s). The time steps present demonstrate important thermal and flow features observed during the thermal flow development.

At H/D = 0.5, Fig 7a shows isotherms and corresponding streamlines during an early heating time, $\tau = 2.27\times 10^{-5}$ (Fig 7a (i)). At this times step, temperature contours show non uniform heating of the fluid body by the direct absorption of solar radiation, and a thermal boundary layer formed above the lower surface. In Fig 7a (ii), the corresponding streamlines indicate flows of low velocity just below the top surface and no bulk flow circulation within the fluid body. The convective flow just below the top surface effectively distributes the heat horizontally; this is achieved in clockwise rotating vortices

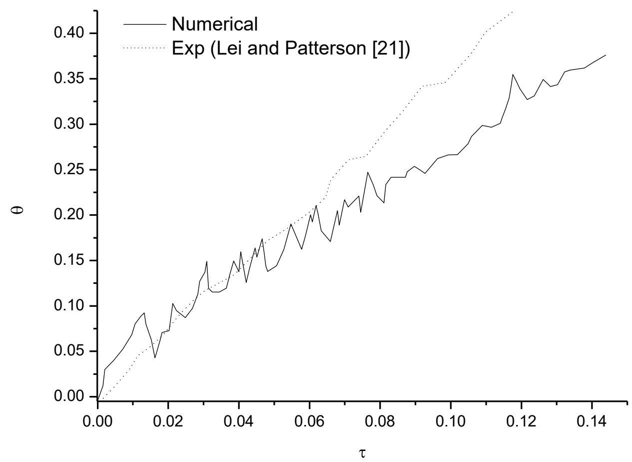

Figure 6: Plot of the time series of temperature in the thermal boundary experiment (dot) and Numerical (solid) layer at (x,y)=(4.25, 0.016).

(Fig 5a (ii)). At a later heating time $\tau = 1.82\times\ 10^{-3}$, Fig 7b(i) shows continuous absorption of radiation results in expansion of the isotherms toward the lower surface. The absorbed heat flux from the lower surface continues to contribute to the boundary layer. thermal boundary layer growth continues during this heating stage until the temperate gradient within the boundary layer reaches a critical value that satisfies the stability criterion for convection. Thermal instabilities are then introduced within the thermal boundary marked by the occurrence of thermal plumes. Streamlines (Fig 7b(ii)) show increased fluid circulation, illustrated by the presence of the circulation cells of varying sizes and strength. Fig 7c(i) shows the thermal and flow features at heating time τ= 3.81$\times$ 10^{-3}. A non linear temperature profile is observed at this time step, where a stratified top layer and a convecting lower stage coexist. Streamlines (Fig 7c(ii)) also show a fully developed unsteady complex flow.

In Fig 8a (i) and (ii) the temperature contours and streamlines at an early time ($\tau = 2.27\times\ 10^{-5}$) is shown for H/D=1. The contours indicate the a non-linear absorption of solar radiation with the fluid body and a developing boundary layer at the lower boundary. Similarly, the corresponding streamlines show a convective flow that distributes the heat horizontally just below the top surface achieved in clockwise rotating vortices (Fig 8a (ii)).

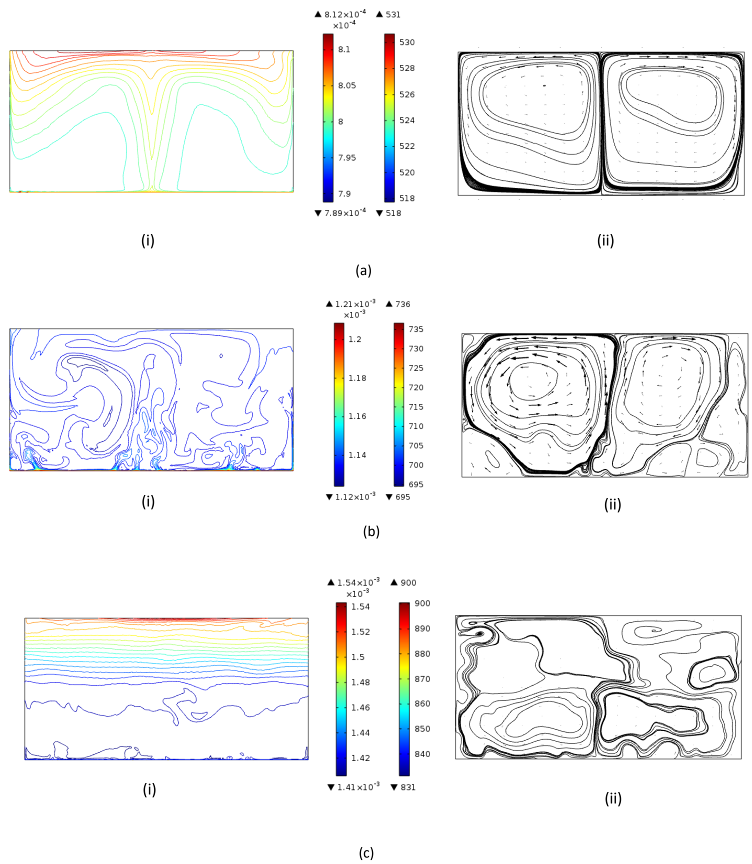

Figure 7: Temperature contours (left) and streamlines (right) for H/D=0.5 (a) $\tau = 2.27\times 10^{-5}$ (b) $\tau = 1.82\times\ 10^{-3}$ (c) $\tau = 3.81\times\ 10^{-3}$

In Fig 8b (i) ($\tau = 1.82\times\ 10^{-3}$), a non linear temperature profile is evident where a stable hot surface layer forms above a thermal plume dominated cooler mixing layer. Streamlines in Fig 8b (ii) indicate no flow in the top fluid layer and unsteady flow in the lower fluid layer. Significant differences between the aspect ratios at H/D= 0.5 and 1 can be seen from the layout of the thermal and flow features and the time scales at which these transitions occur. Fig 8c shows a late heating stage at τ= 3.81$\times$ 10^{-3} (Fig 8c(i)) when the enclosure becomes fully stratified, evident from the nearly parallel isotherms. Streamlines (Fig 8c(ii)) at this time indicate no bulk fluid movement.

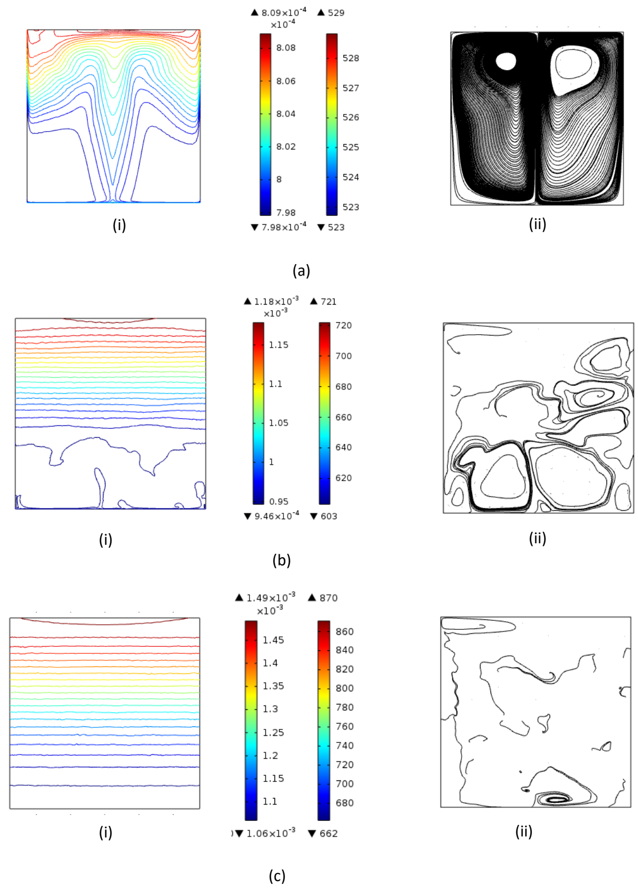

Figure 8: Temperature contours (left) and streamlines (right) for H/D=1 (a) τ = 2.27$\times$ 10^{-5} (b) τ = 1.82$\times$ 10^{-3} (c) τ = 3.81$\times$ 10^{-3}

For H/D= 2, Fig 9a (i) presents the isotherm at the early heating time at τ = 2.27$\times$ 10^{-5}. At later heating times, τ = 1.82$\times$ 10^{-3} (Fig 9b)(i)) and τ= 3.81$\times$ 10^{-3} (Fig 9c (i)); the isotherms have become monotonic and nearly parallel temperature contours illustrating a primarily a conductive heat transfer regime. Corresponding streamlines shows no flows in the lower

boundary in Fig 9b)(i); weak flows of low intensity in the flow solution at 1.82×10^{-3} (Fig 9b)(ii)in the lower layer and weaker flows of much lower intensity at 3.81×10^{-3} (Fig 9c (ii)).
From Fig 7 to Fig 9 it can be seen that resulting temperature profiles and flow patterns that result for a predefined configuration are determined by a complex interaction between the competing stabilisng effect due to the direct absorption of solar radiation, thermocapillary forces and buoyancy forces. The top hot surface layer is generally characterised by no bulk fluid movement [28], however in the current results fluid velocities below the air-salt interface in the horizontal direction are observed. This is attributed to the fact that the interface between a liquid and ambient atmosphere is subjected to very high temperature differences and fluid motion is induced. An identical phenomenon was observed in experiments of Cramer et al.[33] while heating molten salts in a cylindrical cell, heated by heater located just below the top surface. As the induced fluid velocities drive flow along the top surface, and down the lateral wall, in the early stages vortices are formed that are found to be an important mechanism in establishing and maintaining the top surface layer. In the lower mixing fluid layer confined in a depth below the stratified the top hot surface layer consists boundary layer development and thermal plumes. The thermal plumes are observed as important mechanisms for the convective mixing within the lower layer.

4.1. Flow velocity and heat transfer time histories

Figure 10 a-c shows the time history for the vertical flow velocity at a point (x, y)= (0, 0.98H), within the bottom boundary for H/D=0.5, 1 and 2. For the three aspects, the plot for the flow velocity in 10 a, b and c presents the three distinct flow regimes classified as early, transitional and quasi steady marked by i-iii respectively.
In Fig 10a, H/D=0.5, the early flow (i) occurs for $\tau < 3.79\times10^{-5}$ after solar radiative heating is initiated. This flow regime is marked by the development of the diffusive growth of a bottom thermal boundary layer. During this stage the flow velocity smoothly increases from quiescent state to a maximum value corresponding to the initial peak as can be seen in the log scale plot insert in Fig 10a. For heating times $3.79\times 10^{-5} < \tau < 6.73\times10^{-3}$, soon after the initial peak, a sharp drop in the velocity from a maximum value is revealed where after the velocity fluctuates with time in sharp irregular oscillations of varying amplitudes. This marks the transitional stage denoted by (ii)

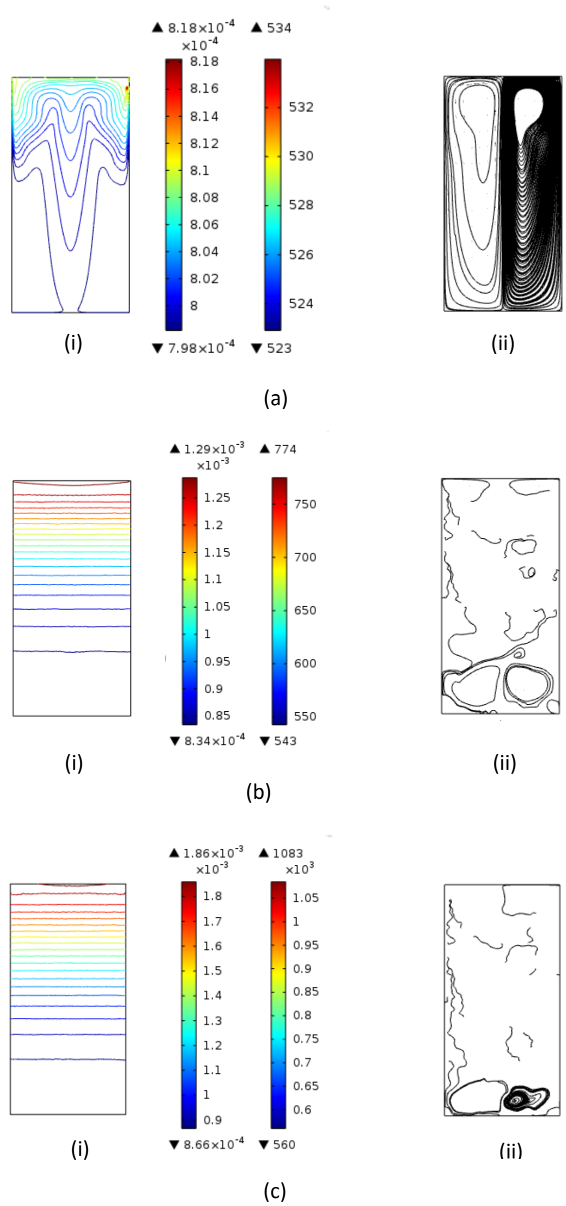

Figure 9: Temperature contours (left) and streamlines (right) for H/D=2 (a) $\tau = 2.27\times 10^{-5}$ (b) $\tau = 1.82\times 10^{-3}$ (c) $\tau = 3.81\times 10^{-3}$

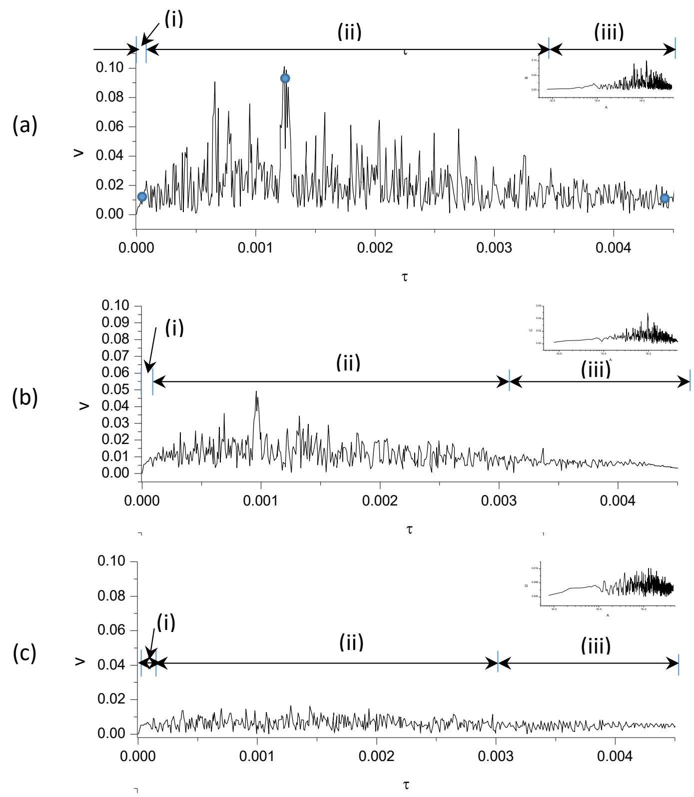

Figure 10: Time series of the flow velocity for H/D=0.5, 1 and 2

marked by the existence of thermal instability (ii). The velocity fluctuations and oscillations with time corresponds to the formation and detachment of rising plumes from the boundary layer. The flow velocity then reaches a quasi-steady state (iii) for heating times $\tau > 6.73 \times 10^{-5}$. During this stage the flow velocity decreases in oscillations and amplitudes which tends to approximately a constant value (Fig 10a). This occurs due to the fluid layer becomes mostly stratified and the convective flow being suppressed and confined within the boundary layer.

Similarly, for H/D = 1 (Fig 10b) and H/D= 2 (Fig 10c), an early (i), transitional (ii), and quasi-steady (iii) flow stages can be easily identified.

The main differences between the aspect ratios are the time scale at which these transitions occur, the magnitude, amplitude and oscillation of fluctuations. These differences can easily be matched with isotherms and streamlines presented in Fig 7 to Fig 9.

The magnitude of the flow velocity and the amplitude of oscillations within the transitional regime decrease with increasing aspect ratio. Time for the occurrence of the first dip that corresponds to change from the initial stage to the transitional stage and thermal plumes initiation is found to shift to higher times with increasing aspect ratio. This is due to an increase in the percentage of the incident radiation absorbed within the salt and reduction in the amount radiation is transmitted to the bottom boundary with increasing aspect ratio. Therefore resulting in lower heating at the bottom boundary at higher aspect ratio. Table 2 presents time scales for identified flow regimes for the respective aspect ratios in Figure 10 a, b and c.

Table 2: Flow regime time scales for H/D=0.5, 1 and 2

	0.5	**1**	**2**
i	$\tau < 8.34\times10^{-5}$	$\tau < 1.14\ \times10^{-4}$	$\tau < 1.29\ \times10^{-4}$
ii	$8.34\times10^{-5} < \tau < 3.12\ \times10^{-3}$	$1.14\times10^{-4} < \tau < 2.93\ \times10^{-3}$	$1.29\times10^{-4} < \tau < 2.52\times10^{-3}$
iii	$\tau > 3.12\times10^{-3}$	$\tau > 2.93\ \times10^{-3}$	$\tau > 2.52\times10^{-3}$

Fig 11 presents the time history for the heat transfer from the lower surface for Ra value of 8.9×10^{11} for H/D=0.5, 1 and 2. Three distinct regions can be seen in Fig 11.

At H/D=0.5, in the early stage which occur for $\tau < 8.34\times10^{-5}$ the heat transfer increases sharply during this stage to a maximum (Fig 11) for all aspect ratios. As no significant flow exists at this stage, heat transfer from the lower plate is dominated by conduction and establishes a thermal boundary layer in the region just above the lower plate. The heat transfer reaches a local minimum at $\tau < 8.34\times10^{-5}$ and then increases into a region of irregular fluctuations before reaching a nearly constant value, where the rate of heat transfer is becomes reduced with reduced fluctuations and amplitude. The presence of the first dip in Fig 11, corresponds approximately to the change from the initial stage to the transitional stage ($\tau < 8.34\times10^{-5}$). The high heat transfer rates in the transition stage correspond to the occurrence of thermal plumes. At the quasi-steady state, the heat transfer decreases due to the increase in bulk fluid temperature. Thus, the transient heat transfer response is characterised by three regimes: conduction in the early flow regime, convection in the transitional stage and quasi steady. The driving mechanisms for heat transfer here can easily be matched with the major fluid developments and features identified from the averaged flow rate in Fig 11. The transient heat transfer at H/D=1 is similar to that at H/D=0.5. The main differences between the two aspect ratios are the time scale at which heat transfer transitions occur and the magnitude. The heat transfer from the lower surface is found to decrease by 55% when the aspect ratio changes from H/D=0.5 to H/D=1. For H/D=2, the sharp spike in the heat transfer at the early stage is observed, where after transcends into a transitional regime with much reduced amplitudes and then into the quasi steady state. Heat transfer at this height is found to decrease by 70% and 30% compared to H/D=0.5 and H/D=1 respectively. The plots reveal features that are consistent with those presented in Fig 10 and the driving mechanisms for heat transfer here can easily be matched with the major fluid developments and features identified from the isotherms and streamlines presented in Fig 7-9.

As a significant consequence of the nonlinear temperature stratification is the

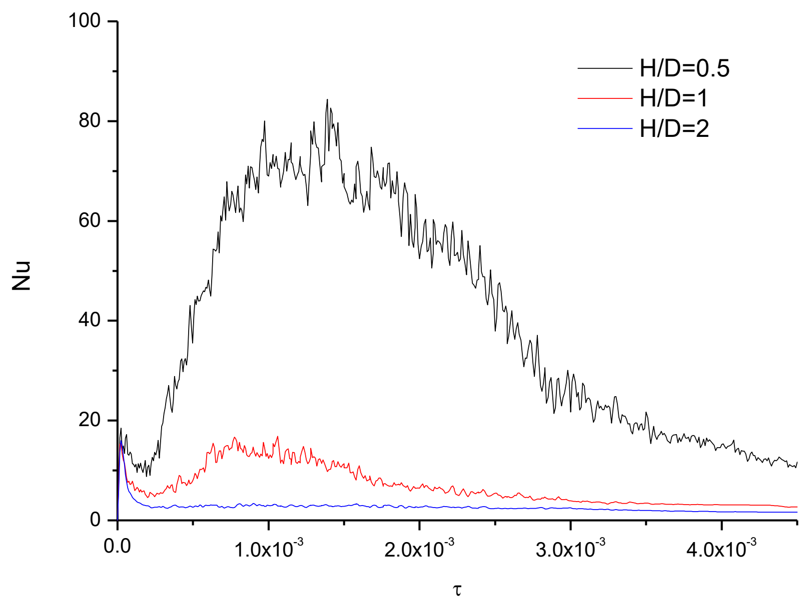

Figure 11: Time series of the heat transfer rate for H/D=0.5, 1 and 2

limitation of the mixing driven by rising thermal plumes with the penetration length scale of the plumes determining the lower mixed layer thickness. It can be seen that the increase in aspect ratio from 0.5 to 2 and stratification is promoted the plume penetration and mixing depth decrease which coincides with the decrease in heat transfer with increasing aspect ratio.

5. Rayleigh number effect on thermal and flow features

In this section the effects of variation of Ra on the heat transfer and fluid flow is examined. Fig 12 shows the time averaged temperature contours, averaged over $\tau = 1.52\times10^{-4}$ to 6.142×10^{-4} in the transitional stage for values: a) Ra=10^7 b) Ra=10^8 c) Ra=10^9 d) Ra=10^{10} e) Ra=10^{11} at H/D=0.5, 1 and 2. At H/D=0.5, it is seen that the plume penetration height and the intensity of plume occurrences increase with increasing values of Ra. The flow in the lower layer exhibits an increasingly complex behaviour with increasing Ra increases. Observations for H/D =1 and 2 reveal that for each aspect ratio increased flows are found to occur with increasing Ra. From these plots it can also be seen that fluid flow corresponding to a particular Ra decreases with increasing aspect ratio.
Fig 13 shows time averaged Nusselt number at the lower boundary at different Ra. It can be seen that heat transfer is dominated by conduction for low Rayleigh numbers (Ra$<10^7$). Convection starts from Ra= 10^7 at H/D=0.5, Ra=10^8 at H/D=1 and Ra$>10^9$ at H/D= 2. The Nusselt number is highest in the shallow domain, H/D =0.5 and lowest at H/D =2. At Ra=10^{10} the heat transfer is lower by 65% for H/D=2 than that for H/D=1 and it is higher by a factor of 1.38 for than that for at H/D=2.

Generally the conduction/transition/convection regimes, as found in cavity flows with differentially heated ends emerge as the Rayleigh number increases. However, the isotherms and streamline obtained here are different from those obtained in differentially heated cavities as extensively presented in [11–13]. The penetrating radiation in the fluid layer which directly heats the fluid in the interior of the cavity destroys the central symmetry of the system that relates the clockwise flow characteristic of natural convection in cavities with differentially heated side walls. The surface layer stability also increases with increasing Ra as indicated at the respective isotherms and streamlines.

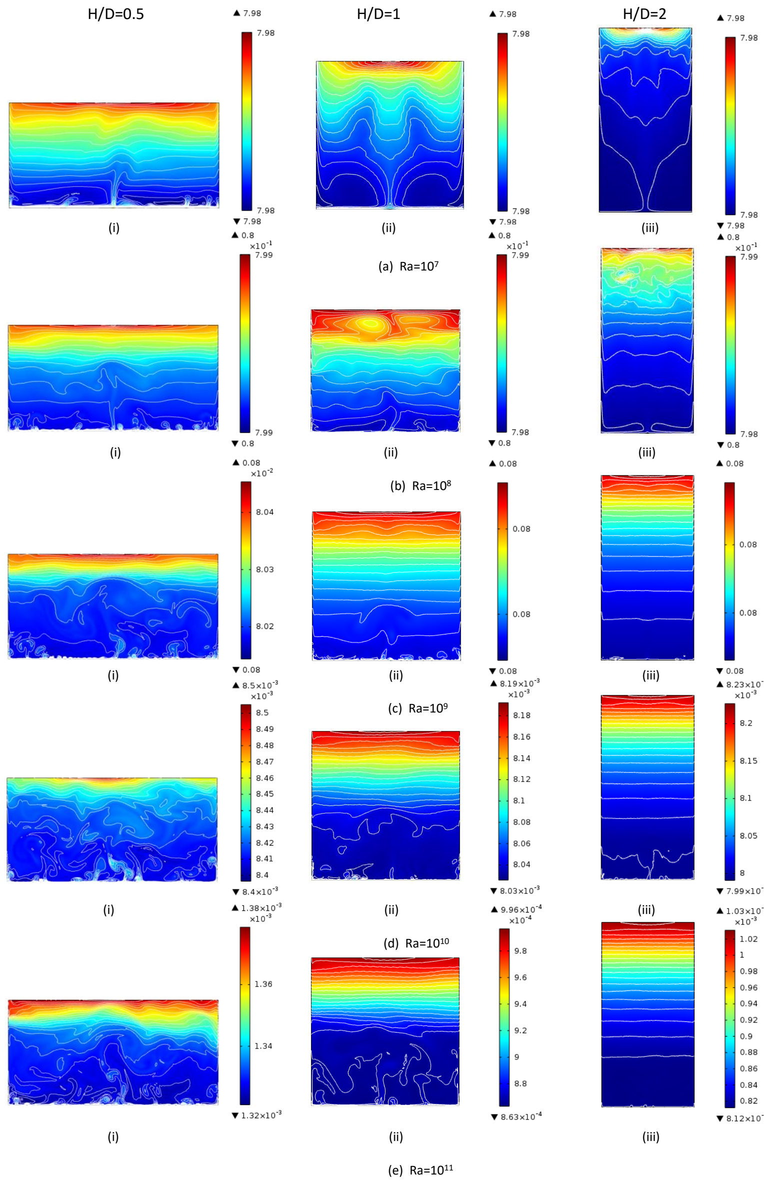

Figure 12: Time averaged temperature contours excluding the quasi steady regime at H/D=0.5 for Rayleigh numbers a) Ra=10^7 b) Ra=10^8 c) Ra=10^9 d) Ra=10^{10} e) Ra=10^{11} for H/D=0.5 (left column), H/D=1 (middle column) and H/D=2 (right column)

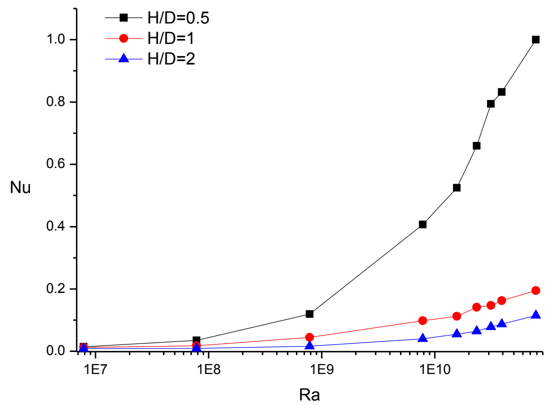

Figure 13: Nusselt number versus the Rayleigh numbers ($10^7 \leqslant \mathrm{Ra} \leqslant 10^{11}$) at H/D=0.5 (black) , H/D=1 (red) and H/D=2 (blue)

6. Conclusion

Two dimensional numerical models have been developed to simulate the transient heat transfer and fluid flow in molten binary KNO_3-$NaNO_3$ salt, directly absorbing concentrated solar radiation. The numerical domain consists of molten binary KNO_3-$NaNO_3$ salt bounded by an open, adiabatic top surface, rigid and adiabatic vertical walls, and a rigid black heat conducting boundary of finite thickness. The developed numerical model accounts for the depth dependent nonlinear volumetric absorption of directly deposited solar radiation based on weighted average values for the solar radiation and the salts attenuation coefficient. The governing equations for the numerical simulations have been carried out using commercial COMSOL Multiphysics software. Numerical simulations were conducted for a charging period of 3 hours used in conjunction with a solar system. Two dimensional numerical results revealed a nonlinear temperature profile consisting of a hot stratified fluid layer lying above a cooler mixing layer. The observed nonlinear temperature was found to occur due to the absorption of radiation within the fluid body being a stabilising force, and the thermal instability at the lower surface being a destablising force. In the top fluid layer Maragoni convection is observed in the region below the top surface, however no bulk flow of fluid is observed. In this layer heat is transferred primarily by conduction. In the lower fluid layer, where convective heat transfer was observed to dominate,

the observed flow regimes are classified into 3 distinct regimes: (1) an initial stage (conduction regime) (2) a transitional stage (evolution of instabilities and onset of convection) and (3) quasi steady state (convective flow).
The average heat transfer is found to decease with increasing aspect ratio from 0.5 to 2 and increase with Rayleigh number. The average heat transfer calculation also revealed that the Nusselt Rayleigh number relationship is not uniformly linear and the average heat transfer number over the lower boundary surface approximately scales with the aspect ratio.
The present study contributes to understanding of the physical processes of solar energy deposition in molten salt necessary in informing rational system design, predict system performance and providing design recommendations necessary for the store to be competitive.

References

[1] Reymond, O., Murray, D.B. and ODonovan, T.S., 2008. *Natural convection heat transfer from two horizontal cylinders.* Experimental Thermal and Fluid Science, 32(8),(1702-1709).

[2] Incropera, F. P, and Lavine, A. S. and Bergman, T. L. and DeWitt, D. P. *Principles of heat and mass transfer*. Wiley, New York, 2013.

[3] Adams, E.E., Wells., S.A *Field measurements on side arms of lake.* J. Hydraul., Eng. 110 (773793), 1984.

[4] Monismith, S.G., Imberger, J., Morison, M.L.. *Convective motions in the sidearm of a small reservoir.* Journal Limnol. Oceanogr., (16761702, 1990.

[5] Slocum, A.H, Codd, D.S, Buongiorno, J., Forsberg, C., McKrell, T., Nave, J.C, Papanicolas, C.N, Ghobeity,A., Noone, C.J, Passerini, S., Rojas, F., Mitsos, A. *Concentrated solar power on demand* Solar Energy, Volume 85, Issue 7, July 2011, Pages 1519-1529, 2011.

[6] Amber, I., O'Donovan, T.S. *Design and operation of a direct solar absorption sensible heat thermal energy storage system.* Conference Proceedings EUROTHERM Seminar No. 98 Concentrating Solar Energy Systems, pp 2013

[7] Peng, Q., Wei, X., Ding, J., Yang, J., Yang, X., 2008. *High-temperature thermal stability of molten salt materials.* International Journal ofEnergy Research 32, 11641174

[8] Delameter W. R, Bergan N. E, *Sandia Report* SAND86-8249. (1990)

[9] Zhou, D., Eames, P *Thermal characterisation of binary sodium/lithium nitrate salts for latent heat storage at medium temperatures.* Solar Energy Materials and Solar Cells Volume 157, Pages 10191025 2016.

[10] Gimeneza, P., Fereresa S. *Effect of heating rates and composition on the thermal decomposition of nitrate based molten salts.* Energy Procedia 69, 2015 pp 654 662

[11] Chandrasekhar, S. *Hydrodynamic and hydromagnetic stability.* Courier Corporation, 2013.

[12] Drazin, P. G. and Reid, W. H. *Hydrodynamic and hydromagnetic stability.* Cambridge university press, 2004.

[13] Ostrach, S. *Natural convection in enclosures.* Journal of Heat Transfer, 110(4b):1175-1190, 1988.

[14] Webb, B.W. and Viskanta, R. *Radiation-induced buoyancy-driven flow in rectangular enclosures: experiment and analysis.* American Society of Mechanical Engineers, Journal of Heat Transfer, 109(2):427-433, 1988.

[15] Webb, B.W. and Viskanta, R. *Analysis of radiation-induced natural convection in rectangular enclosures.* Journal of Thermophysics and Heat Transfer, vol. 1:146-153, 1987

[16] Li, X. and Durbetaki, P. *The conjugate formulation of a radiation induced transient natural convection boundary layer.* International journal for numerical methods in engineering, 35(4):853-870, 1992

[17] Onyegegbu S. *Solar-radiation induced natural-convection in stagnant water layers.* Energy Conversion and Management;30:91-100, 1990.

[18] Verevochkin Y.G., Startsev S.A. *Solar-radiation induced natural-convection in stagnant water layers.* Journal of Fluid Mechanics ;421:293-305, 2000.

[19] Lei,C. and Patterson,J. C. *Unsteady natural convection in a triangular enclosure induced by absorption of radiation*. Journal of Fluid Mechanics;460(4):181-209, 2002.

[20] Lei,C. and Patterson,J. C. *Natural convection in a reservoir sidearm subject to solar radiation: a two-dimensional simulation*. Numerical Heat Transfer: Part A: Applications;42(1-2):13-32, 2002

[21] Lei,C. and Patterson,J. C. *A direct three-dimensional simulation of radiation-induced natural convection in a shallow wedge*. International Journal of Heat and Mass Transfer;46(7):1183-1197, 2003

[22] Coates, M. J. and Patterson, J. C. *Numerical simulations of the natural convection in a cavity with nonuniform internal sources*. International journal of heat and fluid flow; 15,(3):218–225, 1994

[23] Lei,C. and Patterson,J. C. *Natural convection in a reservoir sidearm subject to solar radiation: experimental observations*. Experiments in Fluids;32(5):590-599, 2002.

[24] Coates, M. J. and Patterson, J. C. *Unsteady natural convection in a cavity with non-uniform absorption of radiation*. Journal of Fluid Mechanics:133-161, 1993

[25] Mao, Y. and Lei,C. and Patterson,J. C. *Unsteady natural convection in a triangular enclosure induced by absorption of radiation–a revisit by improved scaling analysis*. Journal of Fluid Mechanics;622(5):75-102, 2009.

[26] Lei,C. and Patterson,J. C. *A direct stability analysis of a radiation-induced natural convection boundary layer in a shallow wedge*. Journal of Fluid Mechanics;480:161-184, 2003

[27] Coates, M. J. and Patterson, J. C. *Characteristics of instability of radiation-induced natural convection in shallow littoral waters*. International Journal of Thermal Sciences:49(1)170–181, 2010

[28] Hattori, T. and Patterson, J.C. and Lei, C. *Mixing in internally heated natural convection flow and scaling for a quasi-steady boundary layer.* Journal of Fluid Mechanics:763 352-368, 2015

[29] Hattori, T. and Patterson, J.C. and Lei, C. *Scaling and direct stability analyses of natural convection induced by absorption of solar radiation in a parallelepiped cavity*. International Journal of Thermal Sciences:88 19-32, 2015

[30] Harfash, A. J. *Three dimensional simulations and stability analysis for convection induced by absorption of radiation*. International Journal of Numerical Methods for Heat & Fluid Flow:25(4) 810–824, 2015

[31] Coastal Chemical Co., LLC. *Hitec Heat Transfer Salt Technical Bulletin, Coastal Chemical Co., LLC.*

[32] Introduction to COMSOL Multiphysics *COMSOL user's guide*

[33] Cramer, A., Landgraf, S., Beyer, E., Gerbeth, G. *Marangoni convection in molten salts* Experiments in Fluids:50(2) 479–490, 2011

[34] Janz, G. J. *Molten salts handbook* Academic Press, 1967

[35] Sohal, S. M. and Ebner, A. M. and Sabharwall, P. and Sharpe, P. *Engineering Database of Liquid Salt Thermophysical and Thermochemical Properties* Report Idaho National Laboratory. 2010

Nomenclature

A	receiver Area	m ^{2}
C	Concentration ratio	
C_p	Heat capacity	$\mathrm{J(kgK)^{-1}}$
D	Diameter	m
g	Acceleration due to gravity	$\mathrm{ms^{-2}}$
H	Height	m
h	Mesh Element size	m
I	Solar irradiation	$\mathrm{Wm^{-2}}$
k	Thermal conductivity	$\mathrm{W(mK)^{-1}}$
κ	Thermal diffusivity	$\mathrm{m^2s^{-1}}$
Nu	Nusselt number	
P	Pressure	Pa
Pr	Prandtl number	
Q	Volumetric heat generation	$\mathrm{Wm^{-3}}$
$\dot{Q}$	Volumetric flow rate	$\mathrm{m^3s^{-1}}$
q	Heat flux	$\mathrm{Wm^{-2}}$
Ra	Rayleigh number	
T	Temperature	K
t	Time	s
u	x velocity component	$\mathrm{ms^{-1}}$
v	y velocity component	$\mathrm{ms^{-1}}$
w	z velocity component	$\mathrm{ms^{-1}}$
y*	Dimensionless height	
α	Absorption coefficient	$\mathrm{m^{-1}}$
τ	Dimensionless time	
μ	Dynamic viscosity	$\mathrm{Nsm^{-2}}$
ν	Kinematic viscosity	$\mathrm{m^2s^{-1}}$
ρ	Density	$\mathrm{kgm^{-3}}$
θ	Dimensionless temperature	